Manuscript File Click here to view linked References

Thin Film Gallium Nitride (GaN) Based Acoustofluidic Tweezer: Modelling and Microparticle Manipulation

Chao Sun[1,2], Fangda Wu[2], Yongqing Fu[3], David J. Wallis[2,4], Roman Mikhaylov[2], Fan Yuan[5], Dongfang Liang[6], Zhihua Xie[7], Hanlin Wang[2], Ran Tao[3], Ming Hong Shen[8], Jian Yang[8], Wenpeng Xun[9], Zhenlin Wu[10], Zhiyong Yang[11], Huaixing Cang[1], Xin Yang[2]

[1] School of Life Sciences, Northwestern Polytechnical University, 710072, P.R. China

[2] Department of Electrical and Electronic Engineering, School of Engineering, Cardiff University, UK CF24 3AA

[3] Faculty of Engineering and Environment, Northumbria University, Newcastle Upon Tyne, UK NE1 8ST

[4] Department of Materials Science and Metallurgy, University of Cambridge, UK, CB3 0FS

[5] Department of Biomedical Engineering, School of Engineering, Duke University, NC 27708-0281, USA

[6] Department of Engineering, University of Cambridge, UK CB2 1PZ

[7] Department of Civil Engineering, School of Engineering, Cardiff University, UK CF24

[8] Preclinical Studies of Renal Tumours Group, Division of Cancer and Genetics, School of Medicine, Cardiff University, UK CF14 4XN

[9] Department of Mechanical Engineering, Northwestern Polytechnical University, 710072, P.R. China

[10] School of Optoelectronic Engineering and Instrumentation Science, Dalian University of Technology, 116023, P.R. China

[11] School of Mechanical Engineering, Tianjin University, 300072, P.R. China

*Corresponding authors:

Dr. Xin Yang, e-mail: YangX26@cardiff.ac.uk and Dr. Chao Sun, e-mail: chaosun@nwpu.edu.cn

ABSTRACT

Gallium nitride (GaN) is a compound semiconductor which shows advantages in new functionalities and applications due to its piezoelectric, optoelectronic, and piezo-resistive properties. This study develops a thin film GaN-based acoustic tweezer (GaNAT) using surface acoustic waves (SAWs) and demonstrates its acoustofluidic ability to pattern and manipulate microparticles. Although the piezoelectric performance of the GaNAT is compromised compared with conventional lithium niobate-based SAW devices, the inherited properties of GaN allow higher input powers and superior thermal stability. This study shows for the first time that thin film GaN is suitable for the fabrication of the acoustofluidic devices to manipulate microparticles with excellent performance. Numerical modelling of the acoustic pressure fields and the trajectories of mixtures of microparticles driven by the GaNAT was performed and the results were verified from the experimental studies using samples of polystyrene microspheres. The work has proved the robustness of thin film GaN as a candidate material to develop high-power acoustic tweezers, with the potential of monolithical integration with electronics to offer diverse microsystem applications.

KEY WORDS

GaN, thin film, SAW, microfluidics, particle manipulation, IDT

1. INTRODUCTION

Surface acoustic wave (SAW)-based acoustic tweezers are recently developed for manipulating micro- [1, 2] and nano-particles [3], cancer cells [4, 5], blood cells and platelets [6, 7], bacteria [8, 9], exosomes [10], droplets [11], lipoproteins [12] and studying intracellular signaling [13]. They show superior advantages and effectiveness as a contactless, label-free, biocompatible, and versatile tool for biomedical applications [14]. Studies have demonstrated improved label-free manipulation efficiency realized by integrating acoustic tweezers with dielectrophoresis [15, 16] and optics [17]. Lithium niobate ($LiNbO_3$) is a commonly used piezoelectric material for fabricating SAW-based acoustic tweezers due to its outstanding electromechanical coupling coefficient. $LiNbO_3$ has a very low thermal conductivity (0.044 W/(cm·K)) [18] which causes challenges for operating the acoustic tweezer at high powers for high-throughput manipulation of biological cells. The high power applied to the interdigital transducers (IDTs) patterned on the $LiNbO_3$ wafer can generate considerable joule heating, which is often not dissipated efficiently through $LiNbO_3$, thus resulting in damage to the $LiNbO_3$ substrate and biological samples [19]. Future acoustofluidic development is desirable to integrate with multi-physical properties such as optoelectronics and semiconductor circuitry for realizing multi-functional lab-on-a-chip (LOC). Since $LiNbO_3$ does not have such a versatility to fulfill this purpose, it is timely to investigate other potential materials with versatile capabilities and robustness for manufacturing acoustofluidic devices.

Gallium nitride (GaN) is one of the key compound semiconductor materials for semiconductor industry after silicon due to its wide band gap, high breakdown electric field, and high electron mobility [20]. These distinct properties make GaN one of the best materials for optoelectronic devices e.g., light-emitting diodes (LEDs), and high power and high-temperature electronics, e.g., high-electron-mobility transistors (HEMT) [21-23]. A comparison of material properties between GaN and $LiNbO_3$ are given in Table 1. Although GaN has a lower effective

electromechanical coupling coefficient which can be compensated by increasing the applied electrical energy, other key attributes such as good thermal conductivity, mechanical, and semiconductor properties of GaN make it a superior material for working in high power, low-loss, harsh environment and integration in a multifunctional platform. GaN possesses good piezoelectric properties and has been applied to make SAW devices for RF filters [24] and resonators [25]. The combination of piezoelectric, optoelectronic and semiconducting properties provides GaN unique opportunities for nano- and microelectromechanical systems (N/MEMS) applications, with a great potential for low cost scaled-up manufacture of monolithic electronic devices using large sizes of GaN wafers [26].

Table 1 Comparisons of properties between GaN and $LiNbO_3$

	Effective coupling coefficient, k^2_{eff}(%)	Acoustic velocity (m/s)	Refractive index	Thermal Conductivity (W/(cm·K))	Elastic Modulus c_{33}(GPa)	Bandgap (eV)	Electron mobility(cm^2/V-sec)
GaN	2 [27]	8044 [20]	2.3-2.5 [29]	1.3 [28]	398 [20]	3.4 [20]	2000 [20]
$LiNbO_3$	5-12 [29]	3900 [20]	2.29 [29]	0.044 [18]	60 [30]	N/A	N/A

Comparing with GaN, there are other types of commonly used thin film piezoelectric materials such as ZnO and AlN, which possess high coupling coefficient and good thermal conductivity to apply in SAW-based microfluidics and LOC applications [29]. AlN-based SAW devices show high leakage current which constrains its applications on high frequencies (e.g. above 10 GHz [31]). Whereas for ZnO, zinc is a dopant of silicon and a contaminant element, which makes ZnO challenging to be integrated with silicon complementary metal-oxide-semiconductor (CMOS) [32]. By applying different dopants of GaN [33] and enhancing photoconductivity through modifying the surface functionalization, GaN can be used to induce physiological responses in yeast [34], improve the adhesion of PC12 cells [35], enhance cell growth [36] and differentiation [37]. As GaN possesses a good biocompatibility, it would be of great interest to investigate the feasibility of using GaN for fabricating SAW devices to manipulate microparticles or biological cells. In addition, GaN can be fabricated as thin film

piezoelectrics with similar benefits as ZnO and AlN for next generation acoustofluidic chips and LOC devices [29]. Thin film GaN-based devices can also overcome the expensiveness and brittleness of bulk $LiNbO_3$ materials and allow SAW functionalities to be realised by depositing the thin piezoelectric film onto wherever the acoustic wave is required [38]. GaN has a higher speed of sound than that of $LiNbO_3$, which allows a GaN-based SAW device to achieve a higher resonant frequency than that of $LiNbO_3$-based device using the same IDT period. In addition, the two-dimensional electron gases on which GaN HEMTs are based, can be used as IDTs to eliminate the mass loading and signal reflection [39]. Such excellent properties along with the maturity of GaN device manufacturing on large wafer sizes makes GaN the perfect choice for next generation SAW devices.

In this study, we developed an acoustic tweezer using thin film GaN, e.g., GaNAT, based on its good thermal and piezoelectric properties. The GaNAT was modelled and tested for patterning and manipulations of microparticles in order to prove the concept of using GaN as an alternative material for manufacturing acoustofluidic devices.

2. MATERIAL AND METHODS

2.1 Fabrication of GaNAT

Fig. 1a shows a photo of the fabricated GaNAT comprising a polydimethylsiloxane (PDMS) microchannel and a GaN-based SAW device. The SAW device was made by a GaN/sapphire wafer patterned with a pair of IDTs, between which the microchannel was bonded to form the GaNAT. The GaN thin film was grown on a sapphire substrate in [0001] direction, and Fig. 1b shows its cross-section image obtained using a scanning electron microscope (SEM, TM4000PLUS, HITACHI, Japan). The GaN and sapphire layers are measured to be ~4.5 μm and ~600 μm thick, respectively. The GaN surface was patterned by bilayers of chromium/gold (30 nm/150 nm-thick) as electrodes using a magnetron sputtering system (LLJGP-560, SKY

technology development, China) after a conventional photolithography process. The GaN wafer was then placed into acetone in an ultrasound bath to perform the lift-off process. Then it was cleaned with ethanol, deionized water and then dried with nitrogen gas. The pitch of the finger electrodes, p, determines the wavelength, λ, of the generated SAW, i.e., $\lambda = 4p$. Both the width and pitch of the finger electrodes are 70 μm, which produce SAWs with a wavelength of 280 μm. Each IDT contains 40 pairs of finger electrodes with an aperture size of 7 mm. The Rayleigh-mode SAW velocity in the GaN/Sapphire is 5,486 m/s in the [0001] direction [40] resulting in a Rayleigh-mode frequency $f = v/\lambda \approx 19.6$ MHz. For the same IDT period, the higher velocity of the GaN/Sapphire allows a higher resonant frequency compared with that of $LiNbO_3$, which could achieve more precise and effective manipulation of the microparticles.

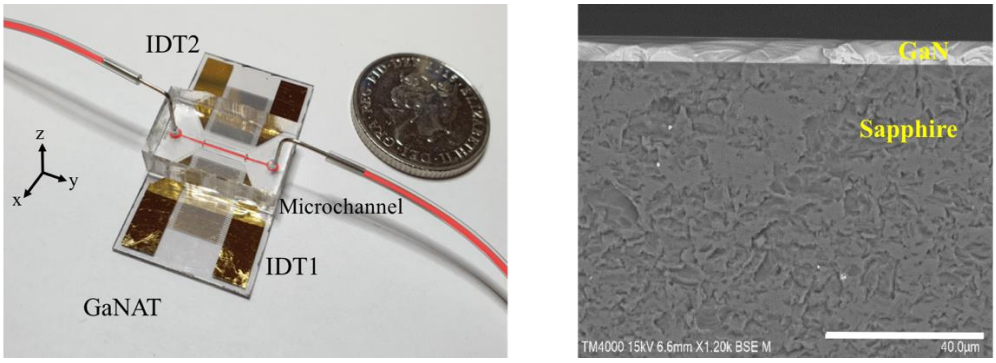

Fig. 1. GaNAT. (a) Photo of the GaNAT device. (b) The scanning electron microscopic image of the undoped GaN film on a sapphire substrate. The scale bar is 40 μm.

The PDMS microchannel with a dimension of 280 μm (W) × 60 μm (H) × 1 cm (L) was fabricated using a standard soft lithography process and a mold-replica procedure. The degassed mixture of the base and curing agent (Dow Corning, UK) with a mass ratio of 10:1 was poured onto the mold, left cured at 65°C for 2 hours to form the microchannel.

2.2 Characterization of GaNAT

The reflection functions of the two IDTs in terms of S_{11} (reflection coefficient) were measured using a vector network analyzer (VNA, E5061B ENA Series, Keysight, US). To reduce the power reflections from the IDTs, impedance matching networks were designed for the IDTs to

maximize the power transmission and reduce the risk of damaging the power amplifier when operated at high powers. The experimental setup is shown in Fig. 2. The radio frequency (RF) signals are amplified by a power amplifier (100A250A, Amplifier Research) to drive the GaNAT. A power meter (U2004A, Keysight Technologies, UK) monitor the real-time incident and reflected powers of each IDT. To quantify the amplitude of SAWs produced on the surface of the GaN thin film with and without the matching networks, a laser vibrometer (PSV-500-VH, Polytec, Germany) was used to measure the vibration on the GaN surface. To investigate the thermal stability of the GaNAT, the temperatures of the two IDTs were recorded using an infrared thermal camera (ETS320, FLIR, US) while changing the input power. For each power, the temperature was measured for three times. The temperature values were recorded two minutes after each power level, when the temperature becomes stabilized.

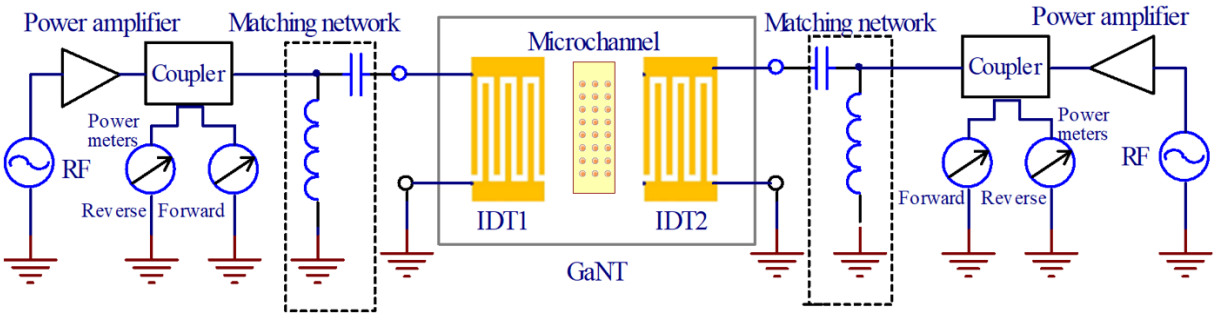

Fig. 2. The experimental setup of the GaNAT.

2.3 Experimental design of particle manipulation

To study particle manipulation using the GaNAT, two batches of mixture polystyrene microspheres samples, e.g., 15 μm and 5 μm, as well as 15 μm and 1 μm, were prepared and injected separately into the microchannel using a syringe pump. When the sample was evenly dispersed inside the microchannel, an RF signal was applied to the GaNAT. The input power of the GaNAT for actuating particles was set to 40 dBm (10W).

3. THEORETICAL and NUMERICAL ANALYSIS

Fig. 3 shows the schematic of the GaNAT consisting of the SAW device and the PDMS microchannel. Applying RF signals to the two IDTs will produce counter-propagating SAWs along the surface of GaN and form standing surface acoustic waves (SSAWs). Once the SAWs interact with the fluid inside the microchannel, leaky SAWs will be produced, thus exerting acoustic radiation force, which is against a drag force on the microparticles inside the microchannel. Along the SSAW propagation, a series of pressure nodes (PNs) with minimal pressure amplitudes and pressure antinodes (ANs) with maximal pressure amplitudes are generated. Microparticles with different signs of acoustic contrast factor $\phi(\beta,\rho)$ are attracted to either PNs (if $\phi(\beta,\rho) > 0$) or ANs (if $\phi(\beta,\rho) < 0$) [41]. $\phi(\beta,\rho)$ is a term determined by compressibility and density given by,

$$\phi(\beta,\rho) = \frac{5\rho_p - 2\rho_f}{2\rho_p + \rho_f} - \frac{\beta_p}{\beta_f} \qquad (1)$$

where $\rho_p, \rho_f, \beta_p,$ and β_f are the densities of the microparticle and the fluid, and the compressibilities of the microparticle and the fluid, respectively.

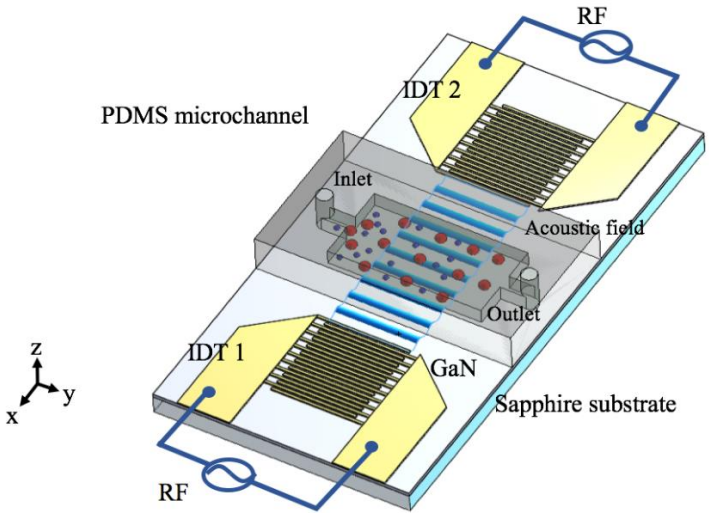

Fig. 3. Schematic drawing of the GaNAT device consisting of a GaN-based SAW device bonded with a PDMS microchannel.

A finite element method (FEM) was applied to analyze vibration modes of the GaN thin film by solving the Newton and Maxwell equations in the two dimensional (2D) model [42]. Using the parameters of the c-orientation GaN in Table S1, the numerical results of the Rayleigh vibration modes of the GaN/sapphire at $\lambda = 280$ μm are obtained which are shown in Fig. S1.

A numerical simulation as described in Ref [43, 44] was further performed to study the acoustofluidic condition of the GaNAT device. COMSOL Multiphysics was used to investigate the acoustic pressure distributions inside the GaNAT device and the particle trajectories within the microchannel. Briefly, the SSAW generates a pressure disturbance in the fluid inside the microchannel. The perturbation induced by acoustic vibration is assumed to be much smaller than the characteristic length scale of the fluid domain [45]. Thus, the perturbation approximation is applied to numerically solve the acoustic pressure and particle velocity. Any particles whose size is much less than the height and the width of the microchannel experience acoustic radiation force $\boldsymbol{F}^{\mathbf{rad}}$ and Stokes drag force $\boldsymbol{F}^{\mathbf{drag}}$ [46],

$$\boldsymbol{F}^{\mathbf{rad}} = -\left(\frac{\pi p_0^2 V_\mathrm{p} \beta_\mathrm{f}}{2\lambda}\right) \phi(\rho, \beta) \sin(2kx) \qquad (2)$$

$$\boldsymbol{F}^{\mathbf{drag}} = 6\pi\mu a\left(\langle \boldsymbol{v}_2 \rangle - \boldsymbol{v}_\mathrm{p}\right) \qquad (3)$$

where p_0,V_p, β_f, λ, $\phi(\rho,\beta)$, k, x, μ, a, $\langle \boldsymbol{v}_2 \rangle$, and $\boldsymbol{v}_\mathrm{p}$ denote acoustic pressure, volume of the microparticle, compressibility of the fluid, wavelength of the SAW, acoustic contrast factor (Eq. 1), wave number, distance from the particle to the closest PN, fluid viscosity, radius of the particle, time-averaged second-order streaming velocity, and velocity of the microparticle, respectively. Using the boundary condition of acoustic impedance (parameters shown in Table S1), $\boldsymbol{F}^{\mathbf{rad}}$ and $\langle \boldsymbol{v}_2 \rangle$ are determined numerically by solving the time harmonic first order- and the second order- acoustic perturbation of the continuous and the Navier-Stokers equations. Generally, the gravitational and buoyancy forces are negligible. Based on Newton's second law of motion, the governing equation for the particle movement can be written [47],

$$\frac{\mathrm{d}\left(m_\mathrm{p}\boldsymbol{v}_\mathrm{p}\right)}{\mathrm{d}t} = \boldsymbol{F}^{\mathbf{rad}} + \boldsymbol{F}^{\mathbf{drag}} \qquad (4)$$

where m_p is the microparticle mass. The net force of the $\boldsymbol{F}^{\mathbf{rad}}$ and $\boldsymbol{F}^{\mathbf{drag}}$ determines the trajectory of the suspended microparticles in the fluid and the microparticles trajectories $\boldsymbol{v}_\mathrm{p}$ can be solved by combining Eqs. 2-4. The inertia of the particles is generally neglected because the

characteristic time of acceleration is small in comparison to the time scale of the motion of the particles [46]. Thus,

$$\boldsymbol{v}_{\mathrm{p}} = \frac{\boldsymbol{F}^{\mathbf{rad}}}{6\pi\mu a} + \langle \boldsymbol{v}_2 \rangle \qquad (5)$$

$\boldsymbol{F}^{\mathbf{rad}}$ and $\boldsymbol{F}^{\mathbf{drag}}$ scale differently with particle radius; $\boldsymbol{F}^{\mathbf{rad}}$ is proportional to the volume of the particles (a^3), whereas $\boldsymbol{F}^{\mathbf{drag}}$ is proportional to the radius of the particles. Thus, a particle transition size, d_c, exists, which determines whether the exerted force on the microparticle is $\boldsymbol{F}^{\mathbf{rad}}$ dominated, i.e., the particle moves towards PNs / ANs when $a > d_c$, or $\boldsymbol{F}^{\mathbf{drag}}$ dominated, i.e., the particle moves in a pattern of streaming vortex ($a < d_c$) [48]. Given the parameters of the above GaNAT, the transition size d_c for the polystyrene microspheres was calculated to be 0.8 μm using the equations in Ref [49]. Microspheres larger than 0.8 μm are driven mainly by $\boldsymbol{F}^{\mathbf{rad}}$ inside the microchannel, otherwise they will be mainly driven by $\boldsymbol{F}^{\mathbf{drag}}$.

4. RESULTS AND DISCUSSION

4.1 The characterization of the GaNAT

The transfer functions of the two IDTs in terms of S_{11} (reflection coefficient) with and without the matching networks are denoted by the solid lines in Fig. 4. The inset shows the zoom-in spectra of S_{11} parameters, where the device shows two peaks at 19.4 MHz and 38.9 MHz corresponding to the Rayleigh and Sezawa modes, respectively. By applying the matching networks, as the S_{11} spectra denoted by the dashed lines, the minimum S_{11} of the two IDTs on Rayleigh mode were reduced from -3.3 dB to -13.2 dB and from -3.6 dB to -14.9 dB, respectively. The addition of the matching networks significantly reduces the power reflection of the IDTs, which can effectively assist the operation of the GaNAT.

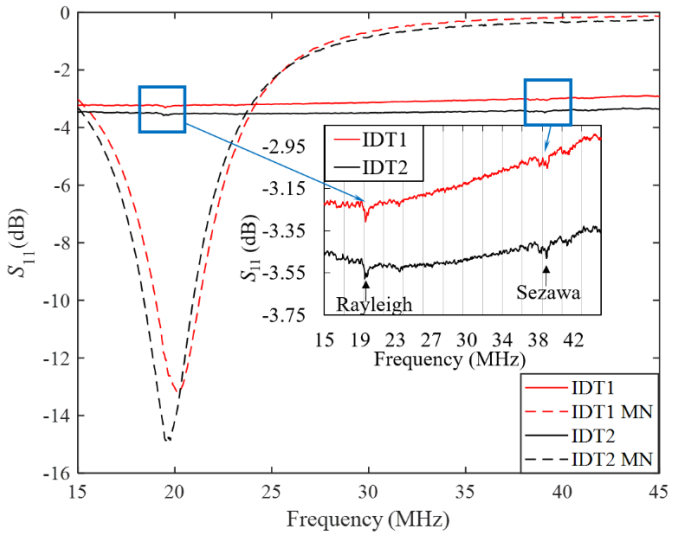

Fig. 4. The reflection parameter (S_{11}) of the GaNAT with the matching networks (MNs) and without the MNs. The inset is the S_{11} spectra of the GaNAT without the MNs, showing both the Rayleigh and Sezawa modes.

Fig. 5 shows the magnitude of SAW vibration produced by the GaNAT with and without the matching networks at various input powers. The use of the matching networks in the GaNAT considerably increased the amplitude of the SAW, e.g. the maximum magnitudes of the SAW at the maximum power of 40 dBm were found to be 220.6 pm and 178.4 pm with and without the matching networks, respectively.

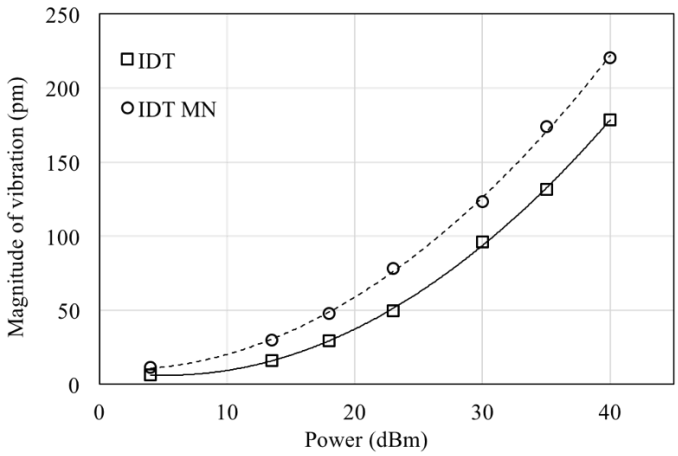

Fig. 5. The magnitude of SAW vibration produced by the GaNAT with and without the MNs.

The relationship between the incident and reflected powers of the GaNAT is shown in Fig. 6, together with the device temperatures at various input powers measured after thermal stabilization. The reflected power accounts for ~3.2% of the incident power which indicates an

efficient energy conversion was achieved by adding the matching networks to the GaNAT [50]. The temperature on the IDTs is found increasing from ~24 °C to ~32 °C when the input power increased from 7 dBm to 40 dBm. The temperature is gradually increased when the applied power is increased (30 dBm to 40 dBm) indicating that the high thermal conductivities of the thin film GaN and sapphire substrate facilitate efficient heat dissipation through the materials. The good thermal stability can simplify system cooling and keep the sample temperature during the operation using the GaNAT below the biological limit.

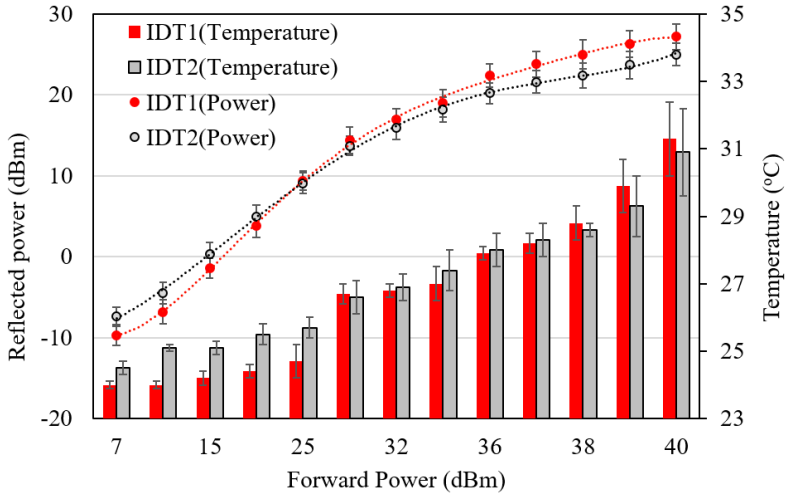

Fig. 6. Power evaluation of the GaNAT shows a high energy conversion on the device when using the matching networks. The temperature rises of the IDTs at different input powers are within the biological limits.

4.2 Numerical analysis of pressure and trajectory of microparticles

As shown in Fig. 7a, three PNs and two ANs are generated inside the microchannel. The corresponding time-averaged second-order velocity $\langle \boldsymbol{v}_2 \rangle$ is shown in Fig. 7b with four streaming vortices formed. This boundary-driven streaming is induced by the substrate vibration with the maximum streaming velocity close to the bottom substrate (the four high velocity regions at the bottom in Fig. 7b). The resultant gradients of the streaming velocity in both *x* and *z* directions lead to the streaming vortex moving from the near field to the far field, and its directions are indicated by the white arrows as shown in Fig. 7b. At the PNs the streaming flows upward while at the ANs the streaming flows downward [51].

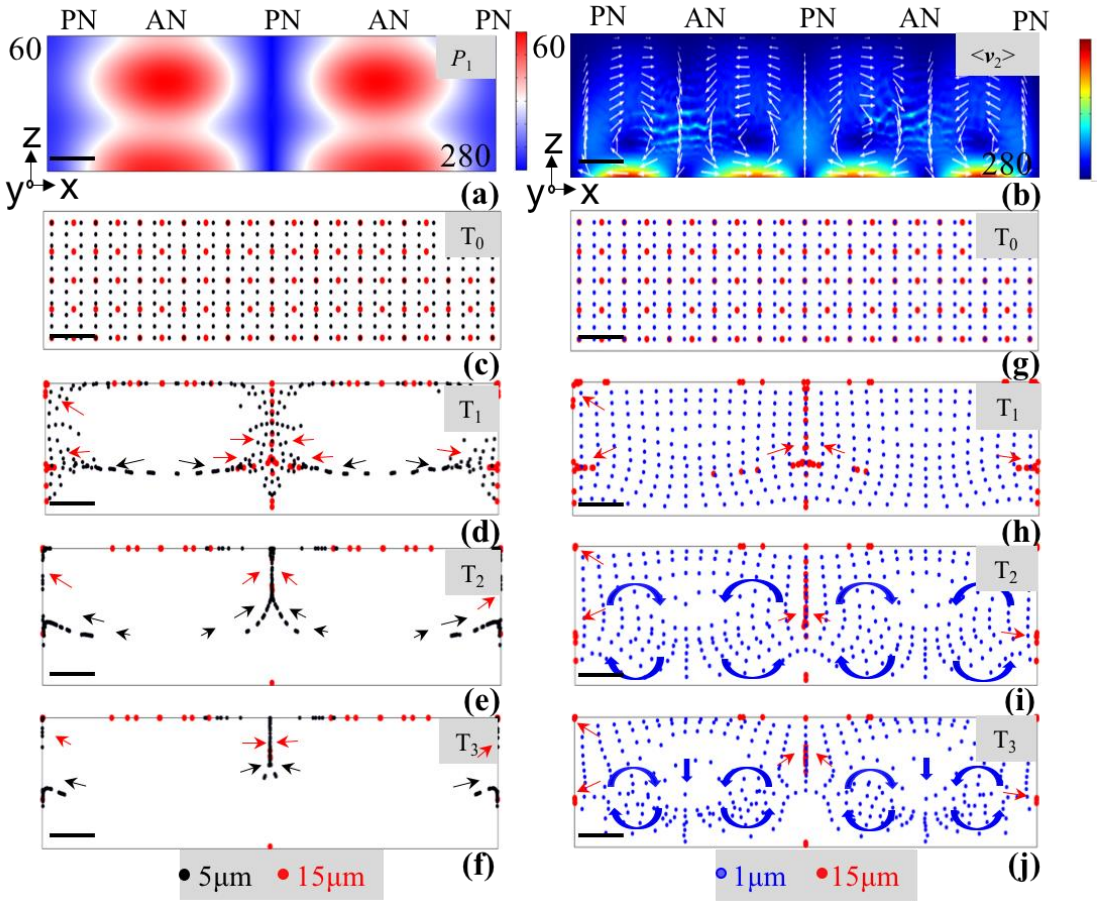

Fig. 7. Numerical simulation of the acoustic pressure, time-averaged second-order velocity and microparticles trajectories of the GaNAT device. (a) The first-order acoustic pressure p_1 inside the microchannel. (b) The time-averaged second-order velocity field $<\boldsymbol{v}_2>$. (c-f) The microparticle trajectories of the mixture of 5 μm (black) and 15 μm (red) at a series of time points. (g-j) The microparticle trajectories of the mixture of 1 μm (blue) and 15 μm (red) at a series of points. The scale bar is 20 μm.

To investigate the trajectory of microparticles with different sizes inside the GaNAT, two batches of microparticle mixtures, e.g., 15 μm and 5 μm, as well as 15 μm and 1 μm, were used for simulation, and the obtained results shown in Figs. 7c-7f, and Figs. 7g-7j, respectively. For the mixture of 15 μm and 5 μm microparticles, since they are both larger than the transition size of 0.8 μm, their motions are mainly driven by the $\boldsymbol{F}^{\mathbf{rad}}$, thus the particles are moving towards the nearest PNs. Two transient moments shown in Figs. 7d and 7e clearly indicate that the 15 μm microparticles are moving faster than 5 μm ones. For example, there are considerable amounts of 5 μm microparticles still moving in the channel while most of 15 μm microparticles

have already arrived at the PNs in the moment shown in Fig.7e. Both the microparticles are able to be aggregated at the PNs as their final positions given enough time as shown in Fig. 7f. Whereas for the mixture of 15 μm and 1 μm microparticles, since the latter ones are very close to the transition size, their motion is driven by both the $\boldsymbol{F}^{\mathbf{rad}}$ and $\boldsymbol{F}^{\mathbf{drag}}$, thus resulting in strong streaming vortex as shown in Fig. 7i, while 15 μm microparticles are already aggregated at the PNs. Results also show that 1 μm microparticles only follow the streaming pattern to achieve partial aggregation phenomenon as shown in Fig. 7j. It is worthwhile noting that the numerical simulation results of the GaNAT show similar streaming patterns as those achieved by acoustofluidic devices made of $LiNbO_3$ working at a frequency of ~6 MHz [46, 47]. The only difference is that a smaller input power is required for the $LiNbO_3$-based SAW devices owing to their large electromechancial coupling coefficient.

4.3 Experimental validation of particle manipulation using GaNAT

For the mixture of 15 μm and 5 μm polystyrene microspheres (Fig. 8a-d), the microscope images were captured on 0 s, 5 s, 15 s, and 1 min after the application of SSAWs. 5 μm microspheres are found to move slower than 15 μm microspheres towards the PNs due to the smaller $\boldsymbol{F}^{\mathbf{rad}}$. This can be seen in Fig. 8b, in which 15 μm microspheres are already aggregated at PNs after 5 s (red arrows) whereas a large number of 5 μm microspheres are still dispersed across the microchannel (black arrows). On 15 s, both sizes of microspheres are aggregated at the PNs with a notable number of 5 μm microspheres are still moving towards the PNs (Fig. 8c). The experimental results show that both sizes of particles can be effectively actuated by the $\boldsymbol{F}^{\mathbf{rad}}$ to migrate towards PNs. Due to their size differences, 5 μm and 15 μm experience different magnitudes of acoustic radiation forces, thus achieving different moving velocities. Most of these microspheres can be found to form three traces of microspheres at the PNs as their final positions at ~1 min, which prove that particles larger than the transition size are

mainly driven by $\boldsymbol{F}^{\mathbf{rad}}$ in the GaNAT. The experimental results are in good agreements with the simulation ones shown in Figs. 7c-7f.

For the mixture of 15 μm and 1 μm microspheres (Fig. 8e-h), most of the 15 μm microspheres are quickly migrated to the PNs after 5 s and well aligned after 15 s (red arrows). However, 1 μm microspheres show no obvious aggregation pattern in 5 s (Fig. 8f) which agrees with Fig. 7h. After 15 s, 1 μm microspheres experience a notable streaming effect and form four streaming vortices as shown in Fig. 8g (see blue arrows). It is worthwhile to note that two traces of 1 μm microspheres are formed next to the center PNs after 1 min (Fig. 8h), which are also well predicted by the simulation as shown in Fig. 7j. The times required to drive different sizes to arrive their final positions are different, which demonstrates the potential of using the GaNAT for separating microspheres or cells with different sizes or mechanical properties. During the experiment, the GaNAT showed its robustness in high power handling and thermal stability, which can benefit for thermophoresis applications with the biological samples.

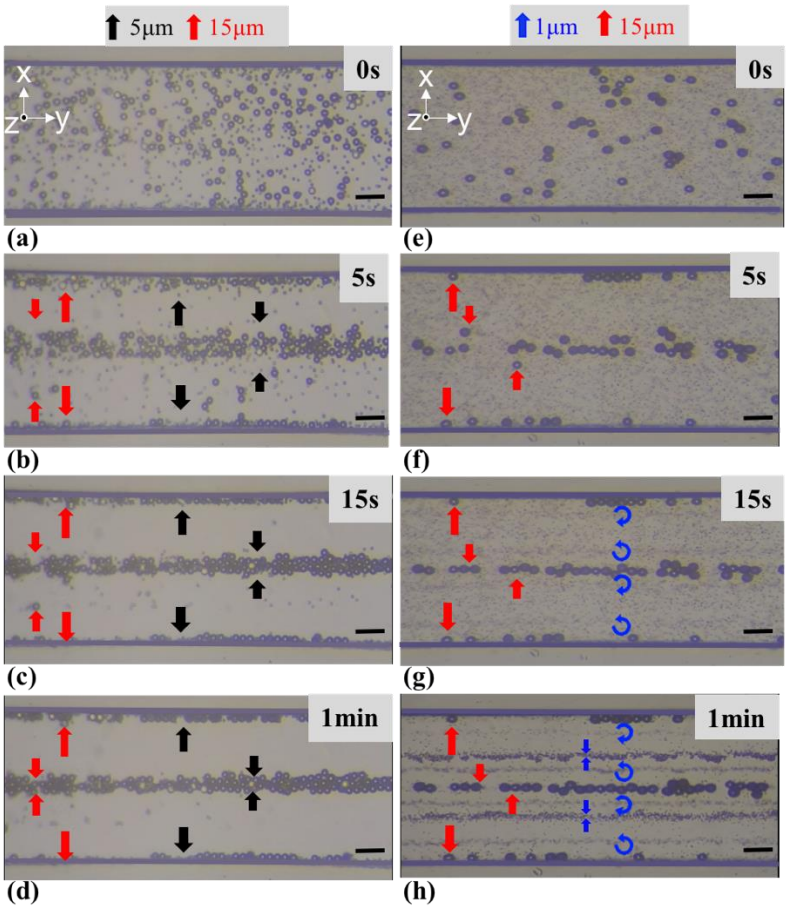

Fig. 8. Experimental results of the mixture of 5 μm and 15 μm polystyrene microspheres and the mixture of 1 μm and 15 μm polystyrene microspheres. (a-d) The distribution of 5 μm and 15 μm microspheres driven by the SSAW field within the microchannel between 0 s to 1 min. (e-h) The distribution of 1 μm and 15 μm microspheres driven by the SSAW field within the microchannel between 0 s to 1 min. The scale bar is 50 μm.

5. CONCLUSION

In summary, for the first time, thin film GaN-based acoustofluidic chip was developed for manipulating microparticles, which proved that GaN is an alternative piezoelectric material for producing SAWs for efficient manipulation of microparticles, despite that the electromechanical coupling coefficient of GaN is lower than that of the $LiNbO_3$. Grown on sapphire, GaN thin film is a thermally robust material for high power SAW generation. By using matching networks, the GaNAT demonstrated efficient SAWs produced on the surface with less power reflected, which is invaluable to handle biological samples when using high input power for high-throughput applications. The thermal performance can be further

improved by replacing the sapphire substrate with either SiC or Si as used in many GaN electronic device applications. The experimental results of particle manipulation using the GaNAT were well predicted by the simulation results. By testing with two mixtures of microspheres, the GaNAT was proven to be able to be used as an acoustic tweezer, and more importantly, with the potential in making acoustofluidic devices to monolithically integrate with compound semiconductors to allow miniature, robust, and multi-physical applications.

ACKNOWLEDGEMENTS

Dr Chao Sun would gratefully acknowledge the financial support from the Natural Science Basic Research Program of Shaanxi Province (Grant No. 2020JQ-233) and Fundamental Scientific Research of Central Universities (3102017OQD116). Prof David J Wallis was funded by Engineering and Physical Sciences Research Council (EPSRC) fellowship (EP/N01202X/2). This work was also funded by EPSRC (EP/P002803/1, EP/P018998/1), UK Fluids Network-Special Interests Group of Acoustofluidics, Global Challenges Research Fund (GCRF), and the Royal Society (IEC/NSFC/170142, IE161019). Dr Zhenlin Wu would like to acknowledge the support from the Natural Science Foundation of China (NSFC) (Grant No. 61704017 and Dalian Science and Technology Innovation Fund (2018J11CY006).

References:

[1] X. Ding, S.C.S. Lin, B. Kiraly, H. Yue, S. Li, I.K. Chiang, J. Shi, S.J. Benkovic, T.J. Huang, On-chip manipulation of single microparticles, cells, and organisms using surface acoustic waves, Proceedings of the National Academy of Sciences of the United States of America, 109 (2012) 11105-11109.

[2] D. Xu, F. Cai, M. Chen, F. Li, C. Wang, L. Meng, D. Xu, W. Wang, J. Wu, H. Zheng, Acoustic manipulation of particles in a cylindrical cavity: Theoretical and experimental study on the effects of boundary conditions, Ultrasonics, 93 (2019) 18-25.

[3] Z. Mao, P. Li, M. Wu, H. Bachman, N. Mesyngier, X. Guo, S. Liu, F. Costanzo, T.J. Huang, Enriching Nanoparticles via Acoustofluidics, ACS Nano, 11 (2017) 603-612.

[4] X. Ding, Z. Peng, S.C.S. Lin, M. Geri, S. Li, P. Li, Y. Chen, M. Dao, S. Suresh, T.J. Huang, Cell separation using tilted-angle standing surface acoustic waves, Proceedings of the National Academy of Sciences of the United States of America, 111 (2014) 12992-12997.

[5] P. Li, Z. Mao, Z. Peng, L. Zhou, Y. Chen, P.H. Huang, C.I. Truica, J.J. Drabick, W.S. El-Deiry, M. Dao, S. Suresh, T.J. Huang, Acoustic separation of circulating tumor cells,

Proceedings of the National Academy of Sciences of the United States of America, 112 (2015) 4970-4975.
[6] Y. Chen, M. Wu, L. Ren, J. Liu, P.H. Whitley, L. Wang, T.J. Huang, High-throughput acoustic separation of platelets from whole blood, Lab on a Chip, 16 (2016) 3466-3472.
[7] A. Shamloo, M. Boodaghi, Design and simulation of a microfluidic device for acoustic cell separation, Ultrasonics, 84 (2018) 234-243.
[8] S. Li, F. Ma, H. Bachman, C.E. Cameron, X. Zeng, T.J. Huang, Acoustofluidic bacteria separation, Journal of Micromechanics and Microengineering, 27 (2017).
[9] Y. Ai, C.K. Sanders, B.L. Marrone, Separation of escherichia coli bacteria from peripheral blood mononuclear cells using standing surface acoustic waves, Analytical Chemistry, 85 (2013) 9126-9134.
[10] M. Wu, Y. Ouyang, Z. Wang, R. Zhang, P.H. Huang, C. Chen, H. Li, P. Li, D. Quinn, M. Dao, S. Suresh, Y. Sadovsky, T.J. Huang, Isolation of exosomes from whole blood by integrating acoustics and microfluidics, Proceedings of the National Academy of Sciences of the United States of America, 114 (2017) 10584-10589.
[11] G. Destgeer, J.H. Jung, J. Park, H. Ahmed, H.J. Sung, Particle Separation inside a Sessile Droplet with Variable Contact Angle Using Surface Acoustic Waves, Analytical Chemistry, 89 (2017) 736-744.
[12] M. Wu, C. Chen, Z. Wang, H. Bachman, Y. Ouyang, P.-H. Huang, Y. Sadovsky, T.J. Huang, Separating extracellular vesicles and lipoproteins via acoustofluidics, Lab on a Chip, 19 (2019) 1174-1182.
[13] J.Y. Hwang, C.W. Yoon, H.G. Lim, J.M. Park, S. Yoon, J. Lee, K.K. Shung, Acoustic tweezers for studying intracellular calcium signaling in SKBR-3 human breast cancer cells, Ultrasonics, 63 (2015) 94-101.
[14] A. Ozcelik, J. Rufo, F. Guo, Y. Gu, P. Li, J. Lata, T.J. Huang, Acoustic tweezers for the life sciences, Nature Methods, 15 (2018) 1021-1028.
[15] Ç. B, Ö. MB, Ç. E, B. S, An integrated acoustic and dielectrophoretic particle manipulation in a microfluidic device for particle wash and separation fabricated by mechanical machining, Biomicrofluidics, 10 (2016) 63.
[16] S.H. Kim, M. Antfolk, M. Kobayashi, S. Kaneda, T. Laurell, T. Fujii, Highly efficient single cell arraying by integrating acoustophoretic cell pre-concentration and dielectrophoretic cell trapping, Lab on a Chip, 15 (2015) 4356-4363.
[17] G. Thalhammer, C. McDougall, M.P. MacDonald, M. Ritsch-Marte, Acoustic force mapping in a hybrid acoustic-optical micromanipulation device supporting high resolution optical imaging, Lab on a Chip, 16 (2016) 1523-1532.
[18] S. Yao, J. Wang, H. Liu, X. Hu, H. Zhang, X. Cheng, Z. Ling, Growth, optical and thermal properties of near-stoichiometric LiNbO3 single crystal, Journal of Alloys and Compounds, 455 (2008) 501-505.
[19] T. Zheng, C. Wang, Q. Hu, S. Wei, The role of electric field in microfluidic heating induced by standing surface acoustic waves, 112 (2018) 233702.
[20] M. Rais-Zadeh, V.J. Gokhale, A. Ansari, M. Faucher, D. Théron, Y. Cordier, L. Buchaillot, Gallium Nitride as an Electromechanical Material, Journal of Microelectromechanical Systems, 23 (2014) 1252-1271.
[21] J. Kuzmik, Power electronics on InAlN/(In)GaN: Prospect for a record performance, IEEE Electron Device Letters, 22 (2001) 510-512.
[22] A.M. Eblabla, X. Li, D.J. Wallis, I. Guiney, K. Elgaid, GaN on Low-Resistivity Silicon THz High-Q Passive Device Technology, IEEE Transactions on Terahertz Science and Technology, 7 (2017) 93-97.
[23] Z. Li, J. Waldron, T. Detchprohm, C. Wetzel, R.F. Karlicek Jr, T.P. Chow, Monolithic integration of light-emitting diodes and power metal-oxide-semiconductor channel high-electron-mobility transistors for light-emitting power integrated circuits in GaN on sapphire substrate, Applied Physics Letters, 102 (2013).

[24] S.H. Lee, H.H. Jeong, S.B. Bae, H.C. Choi, J.H. Lee, Y.H. Lee, Epitaxially grown GaN thin-film SAW filter with high velocity and low insertion loss, Ieee Transactions on Electron Devices, 48 (2001) 524-529.
[25] A. Müller, G. Konstantinidis, V. Buiculescu, A. Dinescu, A. Stavrinidis, A. Stefanescu, G. Stavrinidis, I. Giangu, A. Cismaru, A. Modoveanu, GaN/Si based single SAW resonator temperature sensor operating in the GHz frequency range, Sensors and Actuators, A: Physical, 209 (2014) 115-123.
[26] W.E. Hoke, R.V. Chelakara, J.P. Bettencourt, T.E. Kazior, J.R. Laroche, T.D. Kennedy, J.J. Mosca, A. Torabi, A.J. Kerr, H.S. Lee, T. Palacios, Monolithic integration of silicon CMOS and GaN transistors in a current mirror circuit, Journal of Vacuum Science and Technology B:Nanotechnology and Microelectronics, 30 (2012).
[27] V. Gokhale, Y. Shim, M. Rais-Zadeh, Observation of the Acoustoelectric Effect in Gallium Nitride Micromechanical Bulk Acoustic Filters, 2010.
[28] M.D. Kamatagi, N.S. Sankeshwar, B.G. Mulimani, Thermal conductivity of GaN, Diamond and Related Materials, 16 (2007) 98-106.
[29] Y.Q. Fu, J.K. Luo, N.T. Nguyen, A.J. Walton, A.J. Flewitt, X.T. Zu, Y. Li, G. McHale, A. Matthews, E. Iborra, H. Du, W.I. Milne, Advances in piezoelectric thin films for acoustic biosensors, acoustofluidics and lab-on-chip applications, Progress in Materials Science, 89 (2017) 31-91.
[30] H. Ledbetter, H. Ogi, N. Nakamura, Elastic, anelastic, piezoelectric coefficients of monocrystal lithium niobate, Mechanics of Materials, 36 (2004) 941-947.
[31] Y. Takagaki, P.V. Santos, E. Wiebicke, O. Brandt, H.P. Schönherr, K.H. Ploog, Superhigh-frequency surface-acoustic-wave transducers using AlN layers grown on SiC substrates, Applied Physics Letters, 81 (2002) 2538-2540.
[32] H. Bhugra, G. Piazza, Piezoelectric MEMS Resonators, Spinger, 2017.
[33] P.J. Snyder, P. Reddy, R. Kirste, D.R. LaJeunesse, R. Collazo, A. Ivanisevic, Variably doped nanostructured gallium nitride surfaces can serve as biointerfaces for neurotypic PC12 cells and alter their behavior, RSC Advances, 8 (2018) 36722-36730.
[34] P.J. Snyder, D.R. Lajeunesse, P. Reddy, R. Kirste, R. Collazo, A. Ivanisevic, Bioelectronics communication: encoding yeast regulatory responses using nanostructured gallium nitride thin films, Nanoscale, 10 (2018) 11506-11516.
[35] P.J. Snyder, R. Kirste, R. Collazo, A. Ivanisevic, Persistent Photoconductivity, Nanoscale Topography, and Chemical Functionalization Can Collectively Influence the Behavior of PC12 Cells on Wide Bandgap Semiconductor Surfaces, Small, 13 (2017).
[36] J. Li, Q. Han, X. Wang, R. Yang, C. Wang, Enhanced cell growth on nanotextured GaN surface treated by UV illumination and fibronectin adsorption, Colloids and Surfaces B: Biointerfaces, 123 (2014) 293-301.
[37] C.R. Chen, Y.C. Li, T.H. Young, Gallium nitride induces neuronal differentiation markers in neural stem/precursor cells derived from rat cerebral cortex, Acta Biomaterialia, 5 (2009) 2610-2617.
[38] X.Y. Du, Y.Q. Fu, J.K. Luo, A.J. Flewitt, W.I. Milne, Microfluidic pumps employing surface acoustic waves generated in ZnO thin films, Journal of Applied Physics, 105 (2009).
[39] L.C. Popa, D. Weinstein, 2DEG electrodes for piezoelectric transduction of AlGaN/GaN MEMS resonators, in: 2013 Joint European Frequency and Time Forum & International Frequency Control Symposium (EFTF/IFC), 2013, pp. 922-925.
[40] J. Pedrós, F. Calle, J. Grajal, R.J. Jiménez Riobóo, C. Prieto, J.L. Pau, J. Pereiro, M. Hermann, M. Eickhoff, Z. Bougrioua, Anisotropic propagation of surface acoustic waves on nitride layers, Superlattices and Microstructures, 36 (2004) 815-823.
[41] J. Shi, D. Ahmed, X. Mao, S.C.S. Lin, A. Lawit, T.J. Huang, Acoustic tweezers: Patterning cells and microparticles using standing surface acoustic waves (SSAW), Lab on a Chip, 9 (2009) 2890-2895.

[42] R. Tao, W.B. Wang, J.T. Luo, S.A. Hasan, Y.Q.J.S. Fu, C. Technology, Thin film flexible/bendable acoustic wave devices: Evolution, hybridization and decoupling of multiple acoustic wave modes, 357 (2018).
[43] Z. Mao, Y. Xie, F. Guo, L. Ren, P.H. Huang, Y. Chen, J. Rufo, F. Costanzo, T.J. Huang, Experimental and numerical studies on standing surface acoustic wave microfluidics, Lab on a Chip, 16 (2016) 515-524.
[44] P.B. Muller, R. Barnkob, M.J.H. Jensen, H. Bruus, A numerical study of microparticle acoustophoresis driven by acoustic radiation forces and streaming-induced drag forces, Lab on a Chip, 12 (2012) 4617-4627.
[45] F. Guo, Z. Mao, Y. Chen, Z. Xie, J.P. Lata, P. Li, L. Ren, J. Liu, J. Yang, M. Dao, S. Suresh, T.J. Huang, Three-dimensional manipulation of single cells using surface acoustic waves, Proceedings of the National Academy of Sciences of the United States of America, 113 (2016) 1522-1527.
[46] H. Bruus, Acoustofluidics 7: The acoustic radiation force on small particles, Lab on a Chip, 12 (2012) 1014-1021.
[47] N. Nama, R. Barnkob, Z. Mao, C.J. Kähler, F. Costanzo, T.J. Huang, Numerical study of acoustophoretic motion of particles in a PDMS microchannel driven by surface acoustic waves, Lab on a Chip, 15 (2015) 2700-2709.
[48] R. Barnkob, N. Nama, L. Ren, T.J. Huang, F. Costanzo, C.J. Kähler, Acoustically Driven Fluid and Particle Motion in Confined and Leaky Systems, Physical Review Applied, 9 (2018).
[49] R. Barnkob, P. Augustsson, T. Laurell, H. Bruus, Acoustic radiation- and streaming-induced microparticle velocities determined by microparticle image velocimetry in an ultrasound symmetry plane, Physical Review E - Statistical, Nonlinear, and Soft Matter Physics, 86 (2012).
[50] A. Winkler, R. Brünig, C. Faust, R. Weser, H. Schmidt, Towards efficient surface acoustic wave (SAW)-based microfluidic actuators, Sensors and Actuators A: Physical, 247 (2016) 259-268.
[51] C. Chen, S.P. Zhang, Z. Mao, N. Nama, Y. Gu, P.H. Huang, Y. Jing, X. Guo, F. Costanzo, T.J. Huang, Three-dimensional numerical simulation and experimental investigation of boundary-driven streaming in surface acoustic wave microfluidics, Lab on a Chip, 18 (2018) 3645-3654.